CHAPTER 4

InGaN/GaN Multiple Quantum Wells Nanorods

4.1 Introduction

InGaN/GaN multiple quantum wells (MQWs) are utilized nowadays as the active layers of light-emitting devices based on wurtzite (hexagonal) group III nitrides and also have been attracting much attention as potential materials for short-wavelength light-emitting diodes (LEDs) because of the advantage of tuning ability of the alloy bandgap. Recently, due to the rapid development of fabrication methods for nanostructures, studies of their optical and electronic properties have attracted a great deal of interest for potential applications in optoelectronic devices, such as quantum cryptography, quantum information, and nano-light-emitting devices. For GaN-based nanoscale structures, up to now, the GaN nanorods have been produced by various fabrication methods, such as inductively coupled plasma reactive ion etching (ICP-RIE) without a mask [1], synthesis using carbon nanotubes as templates [2], growth of single-crystal GaN nanorods by hydride vapor phase epitaxy [3] and others. These structures have recently become particularly important for fundamental physical research and potential application. However, all reported methods are relatively complicated and their structures without active layers are not suitable for use in optoelectronic devices. It is possible to produce nanometer-sized nickel (Ni) islands by choosing the correct initial Ni thickness, annealing temperature and annealing time [4].　In this chapter, we present a novel method to fabricate high-density InGaN/GaN MQW nanorods using an ICP-RIE dry etching technique with and without self-assembled nanoscale Ni metal-islands mask. Structural and optical properties were examined with field-emission scanning electron microscopy (FESEM), transmission electron microscopy (TEM) and photoluminescence (PL) measurements.

4.2 Dry etching of III-Nitride materials

GaN and related alloys are finding application for fabrication of blue/green/UV emitters (light-emitting diodes and lasers) and high temperature, high power electronic devices. Due to limited wet chemical etch results for the group-III nitrides, a significant amount of effort has been devoted to the development of dry etch processing [5-8]. Dry etch development was initially focused on mesa structures where high etch rates, anisotropic profiles, smooth sidewalls, and equirate etching of dissimilar materials were required. For example, commercially available LEDs and laser facets for GaN-based laser diodes were patterned

using reactive ion etch (RIE). However, as interest in high power, high temperature electronics [9,10] increased, etch requirements expanded to include smooth surface morphology, low plasma-induced damage, and selective etching of one layer over another occurred. Dry etch development is further complicated by the inert chemical nature and strong bond energies of the group-III nitrides as compared to other compound semiconductors. GaN has a bond energy of 8.92 eV/atom, InN 7.72 eV/atom, and AlN 11.52 eV/atom as compared to GaAs which has a bond energy of 6.52 eV/atom [11]. In this section we will review dry etch processes for the group-III nitrides.

■ *Etch techniques*

a. Plasma etching.

Dry plasma etching has become the dominant patterning technique for the group-III nitrides due to the shortcomings in wet chemical etching. Plasma etching proceeds by physical sputtering, chemical reaction, or a combination of the two often referred to as ion-assisted plasma etching. Physical sputtering is dominated by the acceleration of energetic ions formed in the plasma to the substrate surface at relatively high energies, typically >200 eV. Due to the transfer of energy and momentum to the substrate, material is ejected from the surface. This sputter mechanism tends to yield anisotropic profiles; however, it can result in significant damage, rough surface morphology, trenching, poor selectivity, and nonstoichiometric surfaces thus minimizing device performance. Pearton and co-workers measured sputter rates for GaN, InN, AlN, and InGaN as a function of Ar^+ ion energy [12]. The sputter rates increased with ion energy but were quite slow, <600 Å/min, due to the high bond energies of the group III–N bond.

Chemically dominated etch mechanisms rely on the formation of reactive species in the plasma which adsorb to the surface, form volatile etch products, and then desorb from the surface. Since ion energies are relatively low, etch rates in the vertical and lateral direction are often similar thus resulting in isotropic etch profiles and loss of critical dimensions. However, due to the low ion energies used plasma-induced damage is minimized. Alternatively, ion-assisted plasma etching relies on both chemical reactions and physical sputtering to yield anisotropic profiles at reasonably high etch rates. Provided the chemical and physical components of the etch mechanism are balanced, high resolution features with minimal damage can be realized and optimum device performance can be obtained.

b. Reactive ion etching.

RIE employed both the chemical and physical components of an etch mechanism to

achieve anisotropic profiles, fast etch rates, and dimensional control. RIE plasmas are typically generated by applying radio frequency (RF) power of 13.56 MHz between two parallel electrodes in a reactive gas [see Fig. 4.1 (a)]. The substrate is placed on the powered electrode where a potential is induced and ion energies, defined as they cross the plasma sheath, are typically a few hundred eV. RIE is operated at low pressures, ranging from a few mTorr up to 200 mTorr, which promotes anisotropic etching due to increased mean free paths and reduced collisional scattering of ions during acceleration in the sheath.

Adesida *et al.* were the first to report RIE of GaN in $SiCl_4$-based plasmas [13]. Etch rates increased with increasing dc bias, and were >500 Å/min at 2400 V. Lin *et al.* reported similar results for GaN in BCl_3 and $SiCl_4$ plasmas with etch rates of 1050 Å/min in BCl_3 at 150 W cathode (area 250 in.^{2}) rf power [14]. Additional RIE results have been reported for HBr-, [15] CHF_3-, and CCl_2F_2-based [16] plasmas with etch rates typically <600 Å/min. The best RIE results for the group-III nitrides have been obtained in chlorine based plasmas under high ion energy conditions where the III–N bond breaking and the sputter desorption of etch products from the surface are most efficient. Under these conditions, plasma damage can occur and degrade both electrical and optical device performance. Lowering the ion energy or increasing the chemical activity in the plasma to minimize the damage often results in slower etch rates or less anisotropic profiles which significantly limits critical dimensions. Therefore, it is necessary to pursue alternative etch platforms which combine high quality etch characteristics with low damage.

c. High-density plasma etching.

The use of high-density plasma etch systems including electron cyclotron resonance (ECR), inductively coupled plasma (ICP), and magnetron RIE (MRIE), has resulted in improved etch characteristics for the group-III nitrides as compared to RIE. This observation is attributed to plasma densities which are 2 to 4 orders of magnitude higher than RIE thus improving the III–N bond breaking efficiency and the sputter desorption of etch products formed on the surface. Additionally, since ion energy and ion density can be more effectively decoupled as compared to RIE, plasma-induced damage is more readily controlled. Fig. 4.1(b) shows a schematic diagram of a typical low profile ECR etch system. High-density ECR plasmas are formed at low pressures with low plasma potentials and ion energies due to magnetic confinement of electrons in the source region. Anisotropic etching can be achieved by superimposing an rf bias (13.56 MHz) on the sample and operating at low pressure (5 mTorr) to minimize ion scattering and lateral etching. Pearton and co-workers were the first to report ECR etching of group-III nitride films [17,18]. Etch rates for GaN, InN, and AlN

increased as either the ion energy (dc bias) or ion flux (ECR source power) increased. Etch rates of 1100 Å /min for AlN and 700 Å /min for GaN at 2150 V dc bias in a Cl_2 /H_2 plasma and 350 Å /min for InN in a CH_4 /H_2 /Ar plasma at 2250 V dc bias were reported.

ICP offers another high-density plasma etch platform to pattern group-III nitrides. ICP plasmas are formed in a dielectric vessel encircled by an inductive coil into which rf power is applied [see Fig. 4.1(c)]. The alternating electric field between the coils induces as strong alternating magnetic field trapping electrons in the center of the chamber and generating high-density plasma. Since ion energy and plasma density can be effectively decoupled, uniform density and energy distributions are transferred to the sample while keeping ion and electron energy low. Thus, ICP etching can produce low damage while maintaining fast etch rates. Anisotropy is achieved by superimposing an rf bias on the sample. The first ICP etch results for GaN were reported in a Cl_2 /H_2 /Ar ICP-generated plasma with etch rates as high as ~6875 Å /min [19,20]. Etch rates increased with increasing dc bias and etch profiles were highly anisotropic with smooth etch morphologies over a wide range of plasma conditions. MRIE is another high-density etch platform which is comparable to RIE. In MRIE, a magnetic field is used to confine electrons close to the sample and minimize electron loss to the wall [21,22]. Under these conditions, ionization efficiencies are increased and high plasma densities and fast etch rates are achieved at much lower dc biases as compared to RIE. GaN etch rates of ~3500 Å/min were reported in BCl_3-based plasmas at dc biases < -100 V. The etch result was fairly smooth and anisotropic.

4.3 Fabrication of InGaN/GaN MQWs nanorods

a. Fabrication of InGaN/GaN MQWs nanorods by ICP etching without mask

The nanorods were fabricated from a metalorganic chemical vapor deposition (MOCVD) grown InGaN-based blue LED wafer [23]. The LED structure was grown on a polished optical-grade C-face (0001) sapphire substrate consisting of a 300-Å-thick GaN nucleation layer, a 4-μm-thick Si-doped n-type GaN buffer layer, a 150-Å-thick Si-doped $In_{0.1}Ga_{0.9}N$ wide potential well, ten periods of $In_{0.25}Ga_{0.75}N$/GaN MQWs with a emission photon energy of ~2.56 eV, a 300-Å-thick Mg-doped $Al_{0.15}Ga_{0.85}N$ layer. The In composition was estimated from PL spectra. The thickness for a well and a barrier layer is 60 Å and 120 Å respectively. Finally, a 0.25μm-thick Mg-doped p-type GaN contact layer was grown on top region.

The etching experiment was performed in a load-locked SAMCO RIE 101iPH ICP etch system. Details of the ICP system are schematically illustrated in Fig. 4.2. The ICP power and bias power source with rf frequency were set at 13.56 MHz. Etch gases were Cl_2 and Ar. Both

gases were introduced into the reactor chamber through independent electronic mass flow controllers (MFCs) that can control the flow rate of each gas with an accuracy of about 1 sccm. An automatic pressure controller (APC) was placed near the exhaust end of the chamber to control the chamber pressure. During the plasma etching process, the ICP plasma parameters were held constant at the following conditions: a gas mixture condition of Cl_2/Ar = 10 /25 standard cubic centimeter min (sccm), 200 W ICP source power, 100 W bias power and 1 min etching time. In the Cl_2/Ar plasma, the etched surface morphology was changed dramatically by increasing the chamber pressure, as shown in Fig. 4.3. As the chamber pressure increased, the pillars or nanorods were observed on the surface. The density of the pillars or nanorods is increased with larger chamber pressure. To further investigate the creation of the InGaN/GaN MQWs nanorods, we measured the surface morphology of the etched sample at different etching time as shown in Fig. 4.4. Figure 4.4 shows the SEM image of the etched sample surface at 20, 30, 40 and 50 sec etching time under the etching condition: Cl_2/Ar = 10 /25 sccm, 200 W ICP source power and 100 W bias power. Figure 4.4(a) shows a few pits on the surface after etching of the sample for 20 s. The heights of pits become longer with further etching time in Fig. 4.4(b)-(d) and the variation in the height of the nanorods seems to be related to the etching time under the same etching condition, and the dimension and density of the GaN nanorods have no major change.

Figure 4.5 shows the FESEM image of the fabricated $In_{0.25}Ga_{0.75}N$/GaN MQW nanorods. It is clear that each nanorod has a vertical shape indicating a high selective etching and a good etching performance. The $In_{0.25}Ga_{0.75}N$/GaN MQW nanorods have a near sharp shape on top and a rod body with lateral diameters form 60 nm to 100 nm, heights from 550 nm to 750 nm, as estimated from the SEM image of Fig. 4.5, and obtained a calculated etching rate of about 350 nm /min. Figure 4.6(a) shows the TEM picture of a single $In_{0.25}Ga_{0.75}N$/GaN MQW nanorod. The picture shows evidently portion of the $In_{0.25}Ga_{0.75}N$/GaN MQWs in a straight nanorod with a few-nm-thick p-GaN depending on the material quality of each nanorod and the uniformity of ICP plasma. Structural characterization using double-crystal high-resolution x-ray diffraction confirmed that the MQWs structure in nanorods was intact in structure, as shown in Fig. 4.6(b). The thickness of InGaN well and GaN barrier was estimated to be 6.2 nm and 12.2 nm, respectively, which is in good agreement with the epitaxial design data.

The formation of pillars, nanorods and pits on the etched surface of GaN/InGaN/GaN in the Cl_2/Ar plasma may be attributed to the In-chloride by-products. It is known that boiling points of Ga chlorides and In chiorides are 201 and 600 ^{o}C, respectively [24,25]. Therefore, by-products of In chloride are not volatile in the normal plasma etching process. Figure 4.7

shows this concept for formation of pillars and pits on the surface, and it can be explained by the micromasking of In chlorides and the microtrenching effect of ions [26-28]. If the gas chemistry is Cl_2 /Ar, the plasma begins to etch the MQW layer after the initial etching consumed all the p-GaN layer of about 0.2 μm of the sample. In this stage, since MQWs consist of InGaN/GaN multilayers, two types of by-products can be formed in the Cl_2 /Ar plasma; Ga chloride and In chloride. Because the In chloride is not volatile at the process temperature, it tends to stay on the surface and can become a micromask. Therefore, during further etching of the underneath layer, pillars as shown in Fig. 4.7(a) can be grown by the micromasking effect of these nonvolatile In chlorides. Also, we found that a microtrench was formed at the corner of each pillar bottom. It is because the etch rate near the corners of the pillars is higher compared to the area of no pillars due to the reflection of grazing incident ions from the sidewall of a pillar as shown in Fig. 4.7(b), and this is a typical case of microtrenching. During etching, the growth of pillars was accompanied by microtrenching at the bottom of each pillar, and the microtrenches would grow and undercut more around the bottom of the pillars, which makes the pillars mechanically unstable.

b. Fabrication of InGaN/GaN MQWs nanorods with self-assembled nickel nanomasks

With the recent progress in semiconductor process technology, various nano-structure fabrication methods have been investigated such as e-beam lithography and metal-catalyzed nano-structure synthesis by vapor-liquid-solid growth process on different materials [29,30]. For GaN-based materials, the fabrications and synthesizing of GaN nanowires and nanorods have been reported using various methods, for example carbon nanotube-confined reaction, metal-catalyzed growth assisted by laser ablation, and the high temperature pyrolysis approach and so on [31-33]. Furthermore, using photoenhanced wet etching technique to produce GaN whiskers [34,35] were also reported recently. However, all these reported methods are relatively complicated and mostly using synthesis approach with catalysts assist, and had no mention about the control of dimension and density for these fabricated GaN-based LEDs. We have presented a method to fabricating controllable GaN-based nano-structure using no mask by ICP, but the method caused top-surface of the nanorods being etched and high resistance and not controls the density and diameter. It is possible to produce nanometer-sized nickel (Ni) islands by choosing the correct initial Ni thickness, annealing temperature and annealing time [36]. In this section, we present a novel method to fabricate high-density InGaN/GaN MQW nanorods using an ICP dry etching technique with self-assembled nano-scale Ni metal islands. Structural and optical properties were examined

with field-emission scanning electron microscopy (FESEM), transmission electron microscopy (TEM) and photoluminescence (PL) measurements.

The as-grown wafers were grown by an atmospheric-pressure two-flow metal-organic chemical vapor deposition (MOCVD) system on c-axis sapphire substrates. The substrates were initially treated in H_2 ambient at 1100^oC for thermal cleaning; then a 30-nm-thick GaN nucleation layer was grown at 550^oC. Five periods of $In_{0.15}Ga_{0.85}N$/GaN MQWs were deposited after growing a 3-μm-thick silicon-doped GaN layer on the nucleation layer at 1150^oC. Finally, a 0.1-μm-thick magnesium (Mg) doped GaN layer was grown on top of the $In_{0.15}Ga_{0.85}N$/GaN MQW at high temperature. The well thickness and the In composition in the MQW were determined by X-ray diffraction (XRD) measurements.

The summary processing flowchart for the InGaN/GaN MQW nanorods is shown in Fig. 4.8. First, a 300-nm-thick Si_3N_4 thin film was deposited on the samples by photo-enhanced chemical vapor deposition (PECVD), and then followed by the electron-beam evaporation of a Ni metal film. Then rapid thermal annealing (RTA) at 850^oC for 1 min under nitrogen ambient was used to produce self-assembled nano-sized Ni metal islands on a Si_3N_4 film surface. It should be noted here that an RTA of 1 min was carried out for sufficient time to ensure that all Ni metal islands were isolated and measured by atomic force microscopy (AFM). A RIE was conducted to etch Si_3N_4 film using a gas mixture of CF_4/O_2 to transfer the patterns of nano-sized Ni metal islands to the Si_3N_4 layer. The Ni/Si_3N_4 pillars were fabricated as a nano-mask for the etching process for InGaN/GaN MQW nanorods. The samples were etched down to the n-type GaN layer by ICP-RIE (SAMCO ICP-RIE 101iPH) using a gas mixture of Cl_2/Ar = 50/20 sccm with an ICP source power, a bias power set at 400/100 W and a chamber pressure of 5 mTorr for 3 min of etching time. Finally, the Ni/Si_3N_4 pillars were removed by a buffer oxide etchant to expose the InGaN/GaN MQW nanorods. After all processes, the dimensions and density of the InGaN/GaN MQW nanorods were measured by the FESEM (Hitachi FE-SEM S-5000) and TEM. The optical properties were studied by PL measurements at room temperature. Samples were excited by a 325-nm He-Cd laser line with an excitation power of 25 mW and the emitted luminescence light was collected through a 0.32-m spectrometer with a charge-coupled device (CCD) detector. The best spectral resolution of this measurement system is approximately 1 nm with a grating of 300 grooves /mm.

The morphologies of 150-Å-thick Ni film annealed from 500 to 900^oC for 1 min were determined from AFM measurements (not showed here). We found that no isolated Ni nanoislands were formed below an RTA of 800^oC. RTA at $850\,^oC$ formed isolated Ni metal

nanoislands with a density of about 3×10^9 cm^{-2} observed from morphology measurements. Thus, in this study, RTA of 850°C for 1 min was chosen for the formation of Ni metal nanoislands. The identical fabrication procedure for InGaN MQWs nanorods described above was applied to all samples. It has been reported that the thickness of the initial metal film can play an important role in determining surface morphology at a given annealing temperature [37,38]. Thus, we examined the influence of the initial Ni metal film with thicknesses of 50, 100 and 150 Å to investigate this effect. The mean dimensions and density of InGaN MQW nanorods as a function of thicknesses of initial Ni metal film are shown in Fig. 4.9. The isolated Ni nanoislands form for all samples with different thicknesses of initial Ni film at a RTA of 850°C for 1 min based on surface morphology measurements. In Fig. 4.9, with increasing the thickness of initial Ni metal film from 50 to 150 Å, the nanorod density decreased from 3×10^{10} to 2.2×10^9 cm^{-2} and the nanorods mean dimension increased from 60 to 150 nm. The origin of the decrease in nanorod density may be the increase in the dimensions of Ni metal islands as the initial Ni metal layer increases, resulting in an increase in the mean dimension of the nanorods.

The scanning electron microscope (SEM) image of InGaN/GaN MQW nanorods fabricated by ICP-RIE dry etching with self-assembled Ni metal nano-masks is shown in Fig. 4.10. In the radial direction, the nanorods exhibited a circular geometry indicating an isotropic, homogeneous etch. The rod number density of the nanorods is on the order of $\sim 3.0 \times 10^{10}$ cm^{-2} with a mean lateral dimension range from 60 to 100 nm, depending on the dimension of the nanomasks on the nanorods. The nanorods distribute randomly and the Ni metal nano-masks do as well. A typical TEM (JEOL, JEM-200CX) image of a single InGaN/GaN MQW nanorod is illustrated in Fig. 4.11. The TEM image shows clearly that the five-period MQWs are within the nanorod body. The widths of wells and barriers are estimated to be 5 and 25 nm, respectively, from the growth design. The nanorod is more than 0.28 μm in length based on the TEM image indicating a high-aspect ratio etch. The nanorod has a larger diameter at the top than at bottom, and its sidewalls are sloped and slightly rough. We attribute the imperfect sidewalls and lateral dimensions to mask erosion and ion-damage during the dry etch step.

Taking the room-temperature lattice constant of Ni to be 3.52 Å and that of the corresponding crystalline Si$_3$N$_4$ surface to be 7.61 Å in the a direction and 2.91 Å in the c direction gives the room temperature strain as $\varepsilon_{a(Si3N4/Ni)}$= -53% and $\varepsilon_{c(Si3N4/Ni)}$= 21%, respectively. This indicates that the deposition of Ni on Si$_3$N$_4$ results in a large degree of compression in the a direction and tensile strain in the c direction. Therefore, the formation of

isolated Ni nanoislands on the Si_3N_4 surface was performed during a thermal treatment, which was similar to the result in Ref. 36.

4.4 Optical properties of the InGaN/GaN MQWs nanorods

Optical properties of the nanorods fabricated by mask-less ICP dry etching were investigated by μ-PL system and PLE system, shown in Fig. 4.12 and 3.7, and compared that of the as-grown sample before etching. The samples were placed inside a micro-miniature cryogenic system that can cool down to 80K and 4K by liquid nitrogen and liquid helium. The micro-miniature refrigerator was mounted on a piezoelectric translator stage with a resolution of ~ 2 nm. The samples were excited by a 325-nm laser line of a continued He-Cd laser (25 mW) and the laser beam was focused to a neatly 2 μm spot size in diameter by 15 × objective with an optical resolution of about 1.4 μm. The PL from the samples was collected by the same objective and fed to a 0.32m spectrometer with a spectral resolution of 0.1 nm and a cooled UV-enhanced CCD.

a. Photoluminescence measurement

A cluster of about 16 vertical nanorods was selected from the SEM measurements for base illumination. The measured sample was also placed under the same micro-miniature refrigerator and illuminated with the same excitation power density by translating the piezoelectric translator stage. Figure 4.13 shows the normalized μ-PL spectra of the $In_{0.25}Ga_{0.75}N$/GaN MQWs embedded in nanorods and the as-grown sample at 80K under an excitation power density of approximately 80 W/cm^2. The PL emission peaks of the nanorod and the as-grown sample were estimated from the Gaussian fitting results to be about 2.68 eV and 2.59 eV, respectively. The emission peak of the nanorods showed ~ 90 meV blueshift from that of the as-grown bulk. The full width at half maximum (FWHM) was estimated to be around 89.2 meV which is smaller than 118.3 meV for the as-grown sample. The smaller FWHM could be attributed to the reduction of potential fluctuation effect in the MQWs embedded in the nanometer-sized nanorods. The weak blue emission at ~ 3.02 eV and yellow band emission at ~ 2.2 eV from the spectra of the $In_{0.25}Ga_{0.75}N$/GaN MQW nanorods could be originated from the $In_{0.1}Ga_{0.9}N$ wide potential well layer and n-GaN layer respectively. The inset in Fig. 4.13 is a typical μ-PL emission image at a specific wavelength of 2.68 eV corresponding to the MQW emission energy at room temperature. Therefore, the bright region indicates that the emission originates from the MQWs embedded in the nanorods only, not from the GaN-related materials or from other the excitation source. The dark region has no

MQWs related emission.

InGaN-based III-nitride heterostructures are naturally subjected to a compressive strain because the lattice constant of $In_xGa_{1-x}N$ is inherently greater than that of GaN. For strained MQW structures, the emission peak energies were influenced by the quantum confined Stark effect (QCSE) due to the piezoelectric (PZ) filed, which was found considerably smaller than that of a stress-free $In_xGa_{1-x}N$ epilayers as shown in Fig. 4.15. The built-in macroscopic polarization, which consists of

- ■ The spontaneous polarization due to interface charge accumulations between two constituent materials.
- ■ The piezoelectric polarization due to lattice-mismatch-induced strain.

, plays a significant role in the wurtzite III-nitrides [39-41].

The spontaneous polarization increases with increasing nonideality of the structure, from GaN to InN to AlN, because of the sensitive dependence of the polarization on the structural parameters. In particular, the spontaneous polarization of AlN was found to be only about three to five times smaller than that of typical ferroelectric perovskites. On the other hand, electric polarization fields can be generated by lattice-mismatch-induced strain in strained-layer superlattices of III-V semiconductors. An electric field applied to a QW structure changes the subband energy levels and bound-state wavefunctions in the QW and, hence, the optical transition energies and oscillator strengths, as shown in Fig. 4.16. On the other hand, group III nitrides have very large piezoelectric constants, for instance, e_{31}=-0.57 C/m^2 for InN, -0.22 and -0.49 C/m^2 for GaN, and -0.58 and -0.6 C/m^2 for AlN [39,42,43]. In a previous article, theoretical results showed that the induced piezoelectric field in a strained $In_{0.13}Ga_{0.87}N$ layer grown on (0001)-oriented GaN is expected to be 1.1 MV/cm assuming e_{31}=-0.22C/m^2. Moreover experimental results showed that the photoluminescence peak energy of strained $In_{0.13}Ga_{0.87}N$ QWs was redshifted with respect to that of thick InGaN single layers due to an intrinsic quantum-confined Stark effect (QCSE) caused by the piezoelectric field.

The blueshift in emission peak energy of about 90 meV for InGaN-based MQWs microdisk from the as-grown bulk sample under a laser excitation of 28.3 W/cm^2 was reported earlier, which was attributed to the partial strain relief in the wells [44-46]. The blueshift in PL emission peak of GaN nanorods and GaAs nanowires compared to their bulk materials were also reported and were attributed to the quantum confinement effect [3,38]. The observed blueshift of ~ 90 meV in our result could be the combined contributions of reduction of piezoelectric filed due to partial strain relief and the quantum confinement effect. The amount

of reduced piezoelectric field can be estimated to be around 90 meV/6 nm = 0.15 MV/cm, where 6 nm is the well thickness. Figure 4.16 shows the excitation power-density dependence of peak emission energies on nanorods and as-grown samples at 80K. It is clear that the increases in peak energy with increasing excitation power-density were observed in both samples. This is most likely due to the effects of band filling and carrier screening under high laser excitation, which reduces the strength of piezoelectric field in the wells. These effects have been observed and reported previously [47,48]. In other words, the piezoelectric field was partial reduced in the $In_{0.25}Ga_{0.75}N$/GaN MQW nanorods fabricated by ICP etching. Additionally, the residual piezoelectric field still affects the nanorods on its emission energy even though the strain is relaxed partially. To make a fair comparison, the PL intensity of the nanorods and the as-grown bulk sample was normalized to the area of active region of the 16 nanorods and to the area of the excited active region as well as the size of the laser spot, respectively. The area of active region of a nanorod was estimated to be $\sim 5 \times 10^{-11}$ cm^2 from a diameter of 80 nm. The area of the laser spot was measured to be $\sim 3.1 \times 10^{-8}$ cm^2 from the 2 μm diameter. Additionally, it is taken no account of the sidewall area of the nanorods. Thus, the normalized PL intensity is referred as a PL intensity density in the following. Fig. 4.17 shows that the PL intensity density of nanorods and as-grown bulk sample as a function of excitation power densities at 80K. The PL intensity-density of nanorods was enhanced by a factor of 17 to 24 times compared with that of as-grown bulk sample under various excitation power densities. The enhancement could be attributed to *1.* the enhanced radiative recombination rate due to reduced piezoelectric field. *2.* the smaller absorption length in nanorods. The latter one can be understood because a large fraction of the in-plane propagating light was absorbed in conventional LEDs before reaching the sidewalls. In contrast, light generated from active region within nanorods can escape much more easily and improves the overall light extraction efficiency.

b. Narrow photoluminescence spectra of the InGaN/GaN MQW nanorods

Many research groups have reported that the large compositional fluctuation is due to a large difference in either the lattice constants or the equilibrium vapor pressure of nitrogen between GaN and InN [49,50]. It has been widely proposed that the large compositional fluctuations or phase separation of indium within InGaN/GaN MQWs may give rise to potential minima and QDs-like behavior. In general, the depth of the trap center was found to increase with the indium component. Moreover, spontaneous emission efficiency of InGaN/GaN MQWs has been recognized to be controlled by a balance between the exciton

localization and wavefunction separation due to the QCSE, which result from electric field F normal to the QW plane owing to spontaneous and piezoelectric polarizations [51-53]. However, it has still not been confirmed that the photoluminescence (PL) spectra of InGaN/GaN MQWs consists of sharp and discrete lines. This is because quantum-confined structures in MQWs have slightly different sizes and compositions, or the period of compositional fluctuations is too short, leading to the observation of broad linewidth spectra. Therefore, the luminescence signals of individual potential minima can not be observed easily. Recently, we have reported the fabrication of GaN-based nanorods by inductively coupled plasma (ICP) etching [54,55]. The etching process and sample growth were mentioned in above section. The optical properties of the nanorods were investigated by a micro-photoluminescence (μ-PL) setup. For PL measurement, a doubled Ti: Sapphire laser operating at 390 nm with a spot diameter of 40 μm and a liquid helium flow cryostat for low temperature were employed.

A typical PL spectrum of InGaN/GaN nanorods under an excitation density of 0.9 W/cm^2 was measured at 4K as shown in Fig. 4.18. It consists of several discrete emission peaks whose positions are at 449, 453 and 457 nm, respectively. The strong narrow emission peak at 457 nm has a full width at half maximum (FWHM) of about 1.5 nm. The position difference between each peak is estimated to be 4 nm (24 meV). The insert in figure 4.18 is the spectrum from the as-grown bulk wafer before ICP etching, which was measured at the same condition for the nanorods. It shows a typical InGaN/GaN MQWs spectrum with a FWHM of about 26.5 nm and an undulation behavior which is probably due to the Fabry-Perot interferences within the epitaxial layers [56]. Indeed, fabrication of nanorods structure from the In$_{0.3}$Ga$_{0.7}$N/GaN MQWs bulk wafer does exactly show the different behavior than the typical PL emission spectra of bulk MQWs. This could be due to the decrease of in-homogeneous broadening in wells of nanorods as shown in Fig. 4.19.

An increase of the excitation density usually results in a pronounced and continuous blueshift of the in-homogeneously broadened PL spectra of InGaN/GaN MQWs, and there is still debatable discussion concerning the relative importance of bandtail filling and screening of internal electric field such as piezoelectric field induced by strain energy. The situation appears completely different, if one looks at the excitation power dependent PL spectra of InGaN/GaN MQWs embedded within small nanostructures. Figure 4.20 shows a series of spectra record at different excitation densities between 0.9 and 10.1 W/cm^2 for In$_{0.25}$Ga$_{0.65}$N/GaN MQWs nanorods at 4K. Under low excitation densities, the e_1-h_1 peak at 457 nm is dominant. However, with increasing excitation density, the intensity of peak on the

high-energy side of the e_1-h_1 peak increases. Finally, this peak at 453 nm becomes dominant over the e_1-h_1 emission. It have been demonstrated that the existence of three-dimensionally localized, QDs-like states/structure from the appearance of individual spectrally narrow emission lines and high-resolution transmission electron microscopy analysis in high indium composition (x> 20%) InGaN/GaN MQWs [50, 57]. Thus, this is most likely the feature of QDs-like due to carrier localization and more efficient recombination through localized states [58]. On the other hand, the single exciton recombination peaks do not show any energy shift with increasing excitation power, demonstrating that no variation of the ground state energy due to screening by free carriers occupying delocalized states occurs. It also suggests that excitons are strongly confined in quantum dots-like region or localization centers.
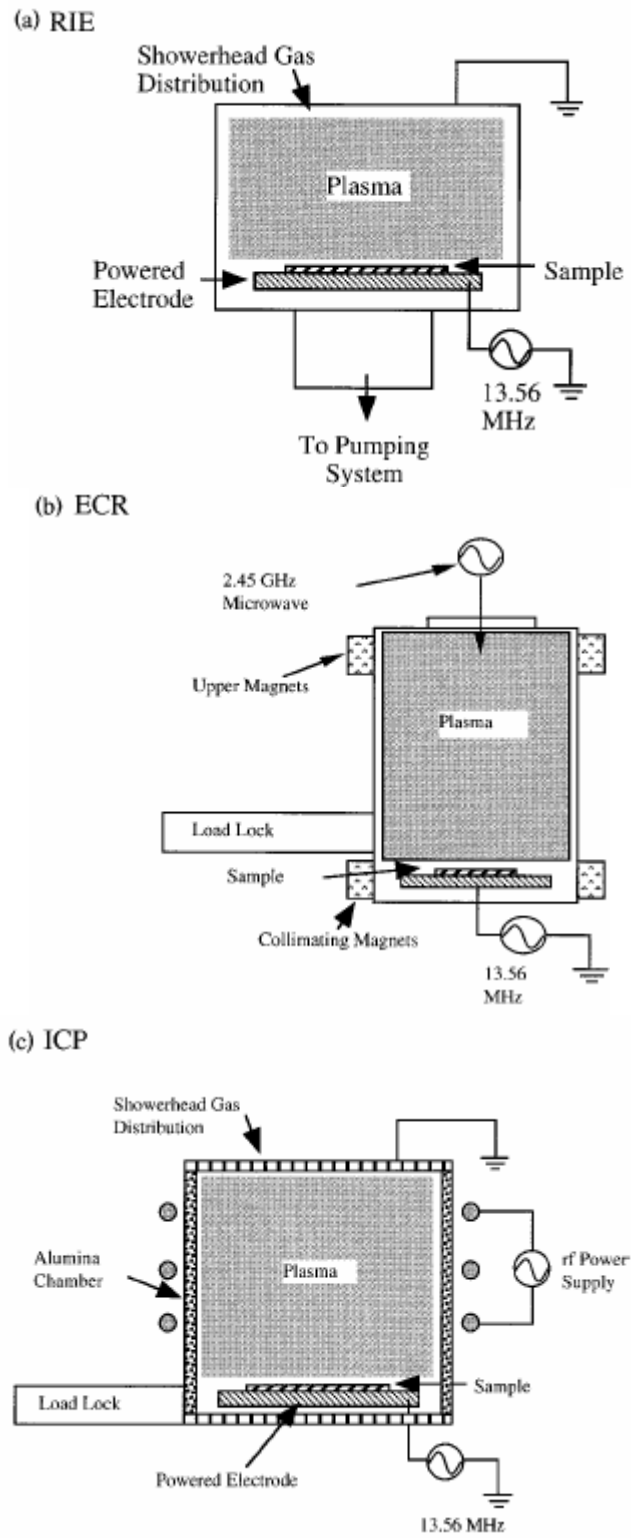
Fig. 4.1. Schematic diagram of (a) RIE, (b) ECR, and (c) ICP etch platforms.
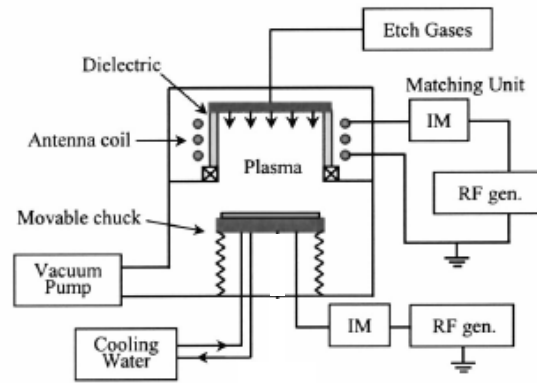
Fig. 4.2. Schematic illustration and photo of the ICP etch system.
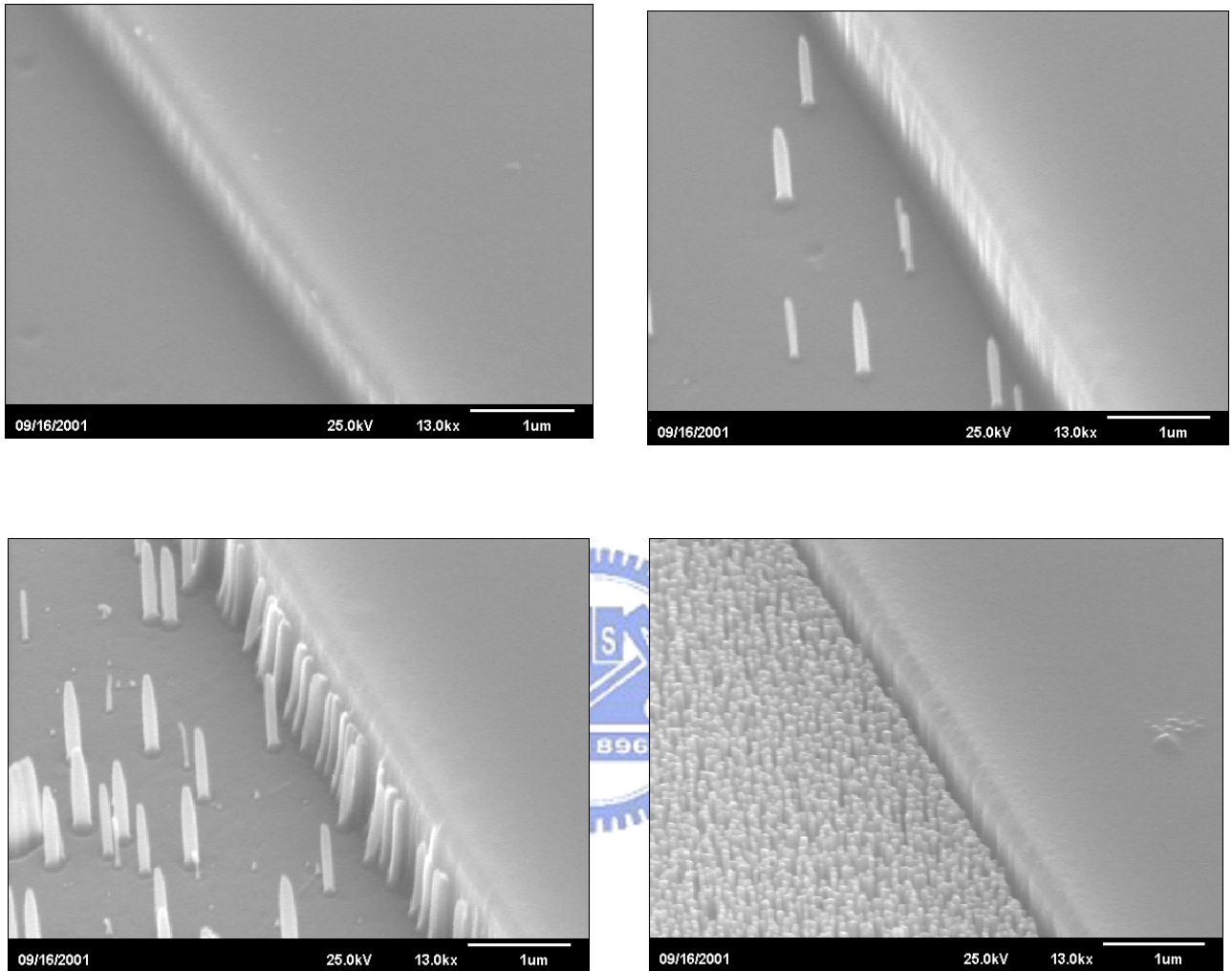
Fig. 4.3. SEM images of the InGaN/GaN MQWs nanorods at different chamber pressures : (a) 2.5 mTorr, (b) 20 mTorr, (c) 30 mTorr, and (d) 40 mTorr.
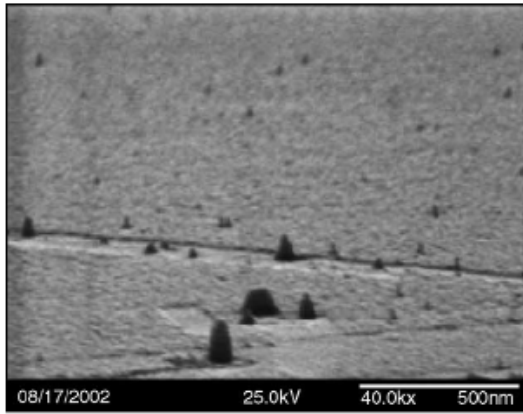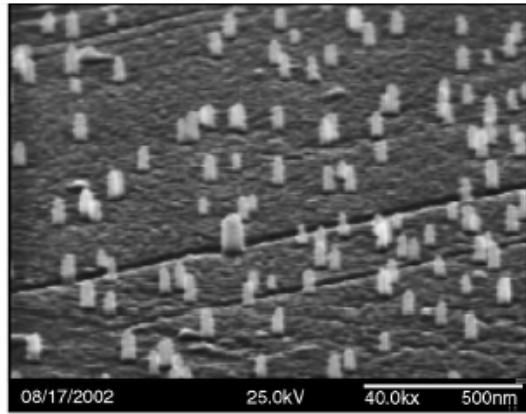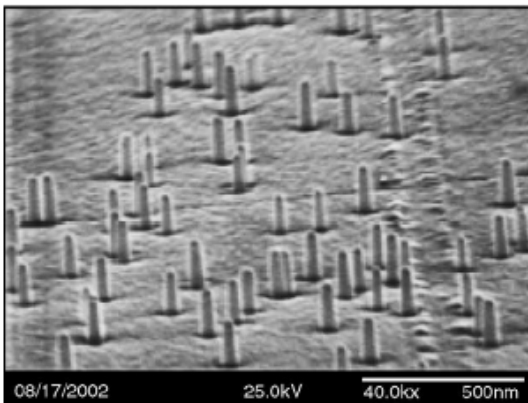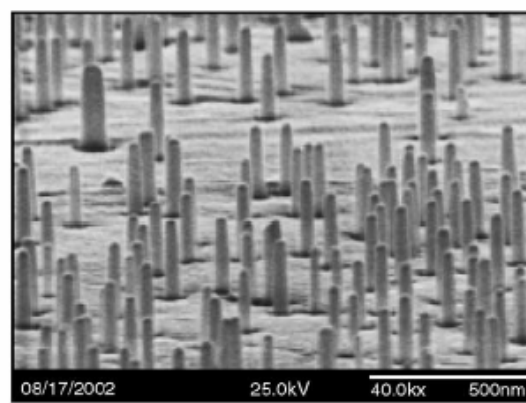
Fig. 4.4. SEM images of InGaN/GaN MQWs nanorods at various etching time: (a) 20 s, (b) 30 s, (c) 40 s and (d) 50 s.
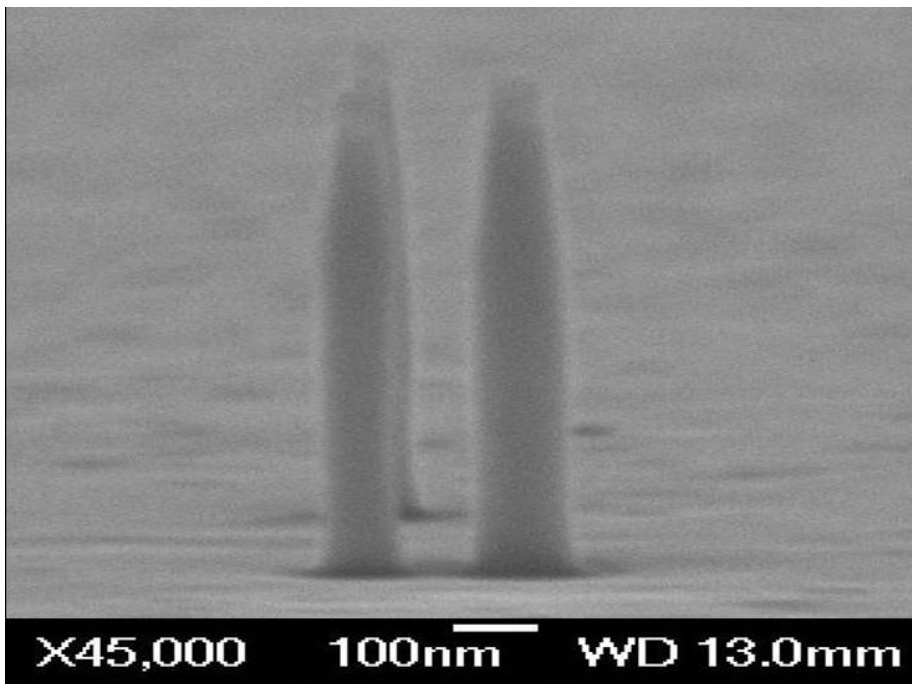
Fig. 4.5. SEM images of the InGaN/GaN MQWs nanorods fabricated by ICP dry etching.
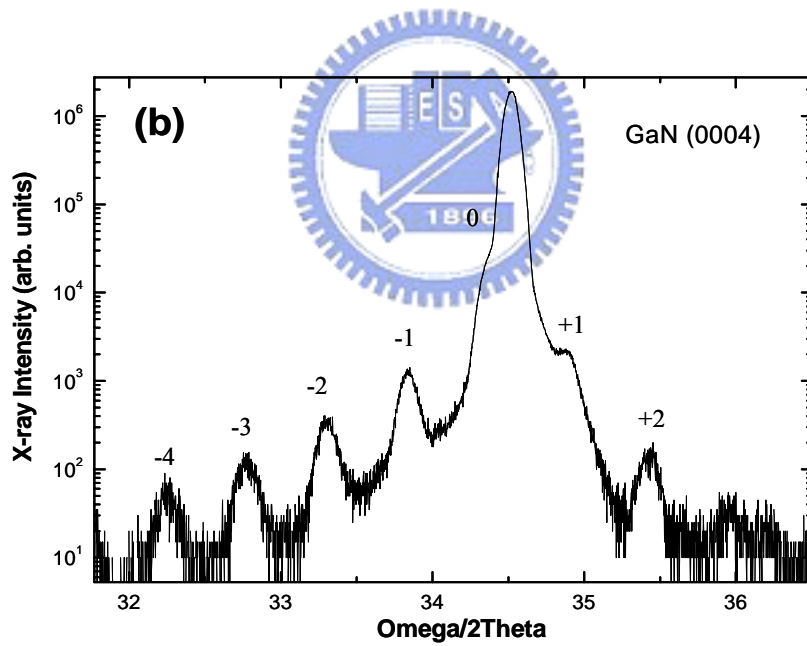
Fig. 4.6. (a) Transmission electron micrograph of a single InGaN/GaN MQWs nanorod. (b) Double-crystal x-ray diffraction spectra omega/2theta scans of the InGaN/GaN MQWs nanorods.
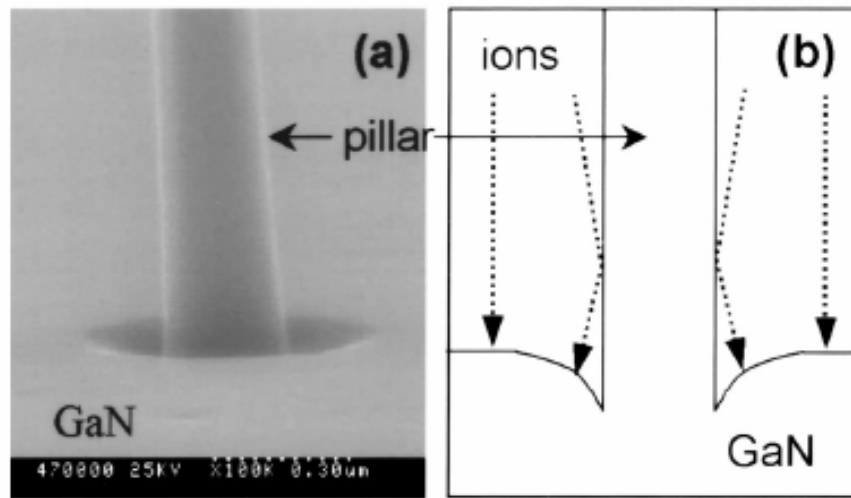
Fig. 4.7. Formation of nanorods and pits on the GaN surface agter etching in Cl_2/Ar plasma [26-28].
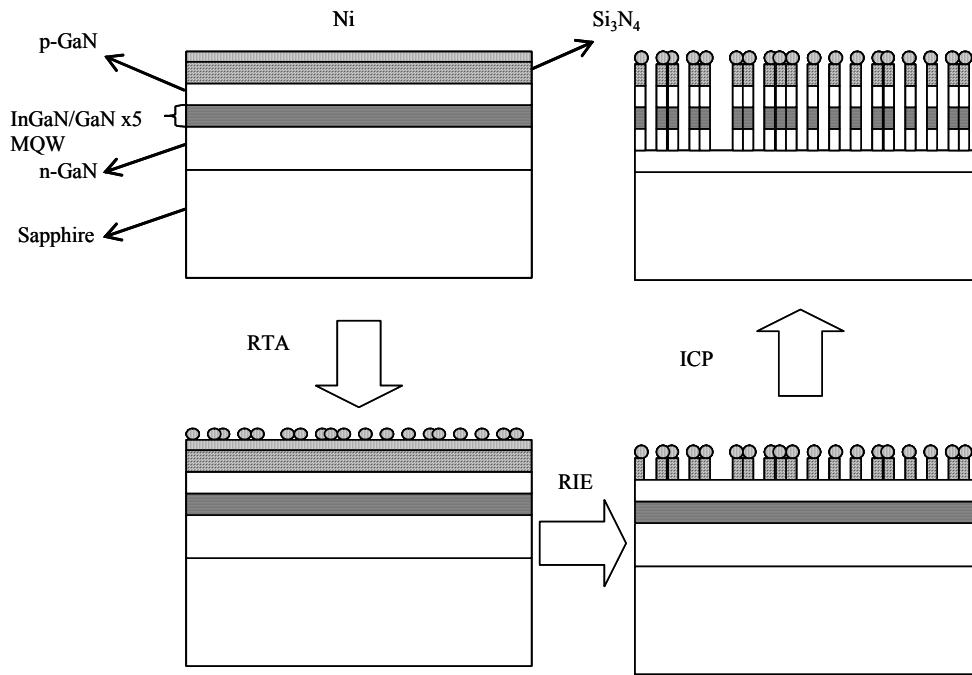
Fig. 4.8. Schematic processing flowchart for InGaN/GaN MQW nanorods.
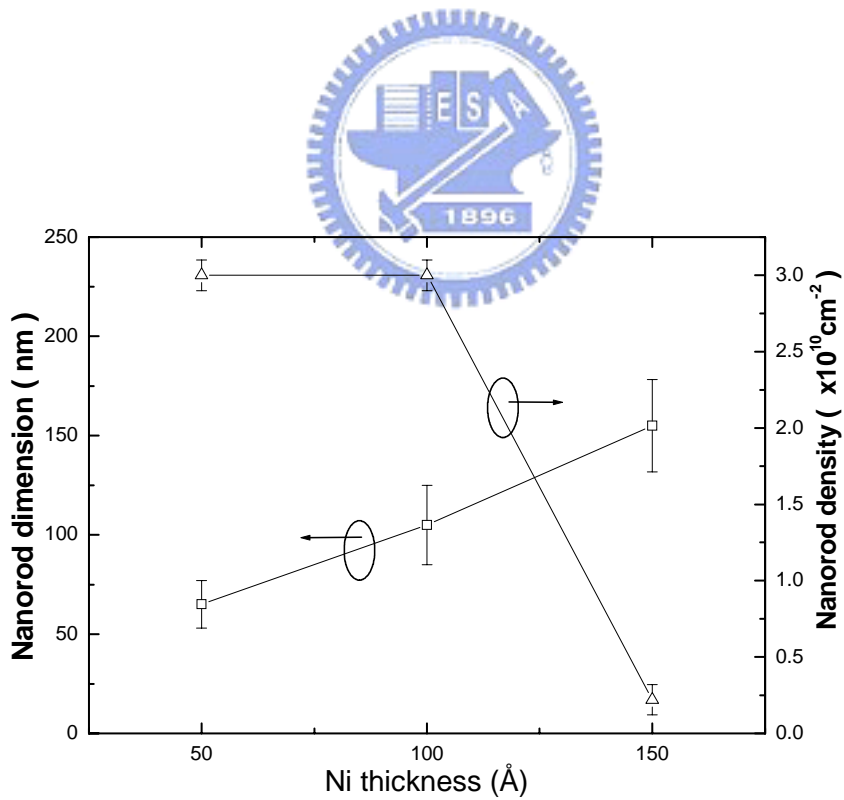
Fig. 4.9. Mean dimensions and rod number density of InGaN MQW nanorods as functions of thickness of initial Ni metal film from 50 to 150 Å.
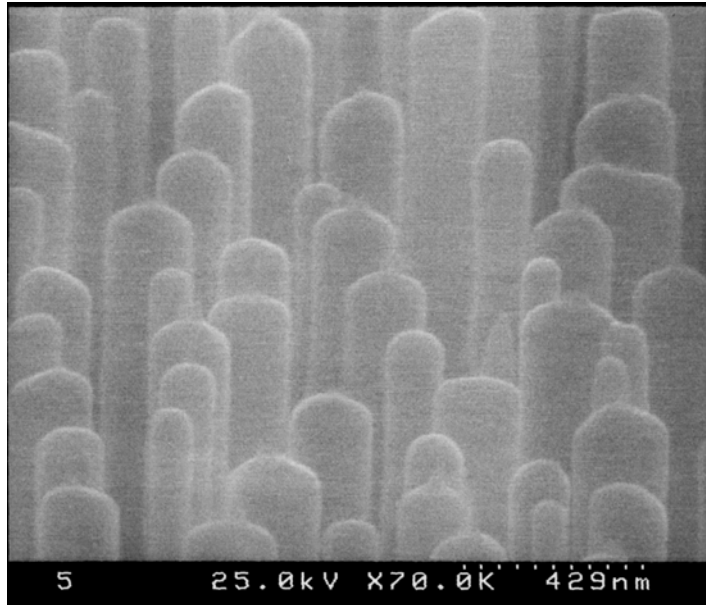
Fig. 4.10. SEM image of InGaN/GaN MQW nanorods fabricated by ICP-RIE dry etching with self-assembled Ni metal nano-masks.

0.1 μm p-GaN

InGaN/GaN (5/25 nm) *x* 5 MQW
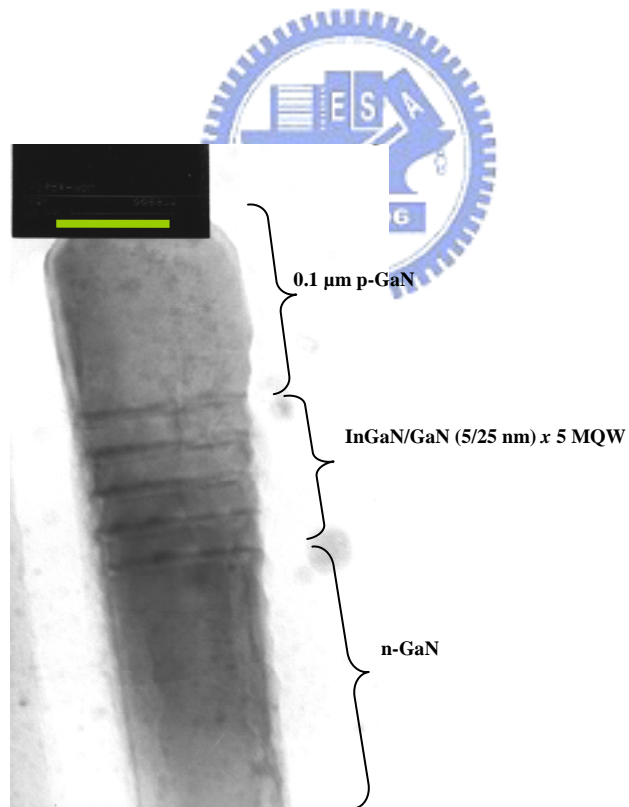
n-GaN

Fig. 4.11. TEM image of a single InGaN/GaN MQW nanorod.
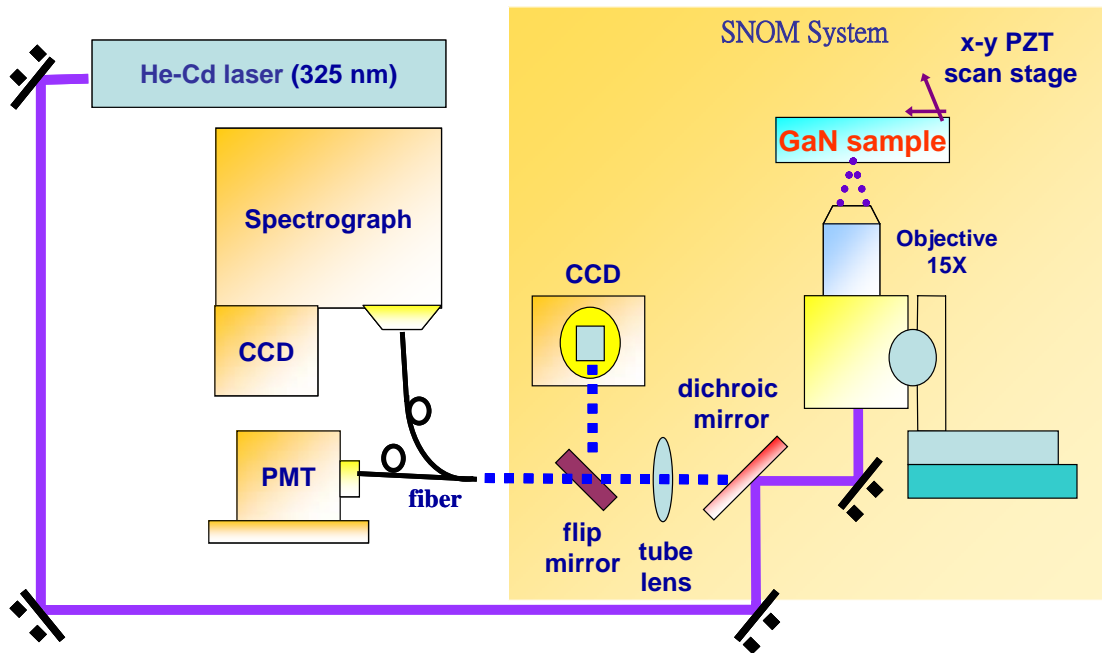
Fig. 4.12. Setup diagram of μ-photoluminescence system.
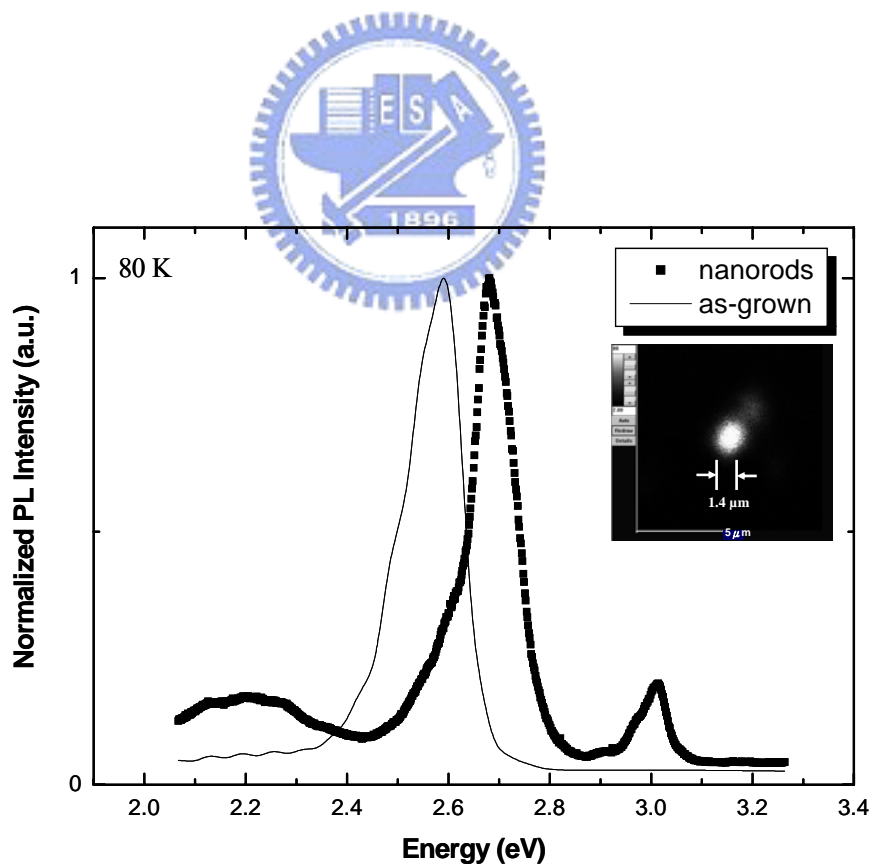
Fig. 4.13. 80K μ-PL spectra of the In$_{0.25}$Ga$_{0.75}$N/GaN MQW nanorods and as-grown MQW sample. The inset is a scanning confocal μ-PL image at RT of a cluster of nanorods at a specific energy of 2.61 eV.
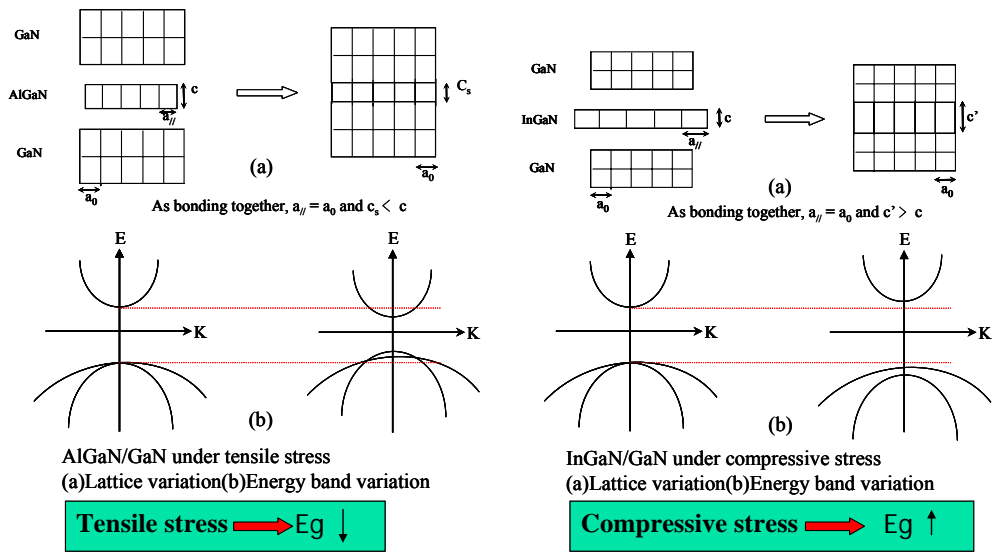
Fig. 4.14. Influence of tensile and compressive stress on E-K diagram of nitride-based materials.
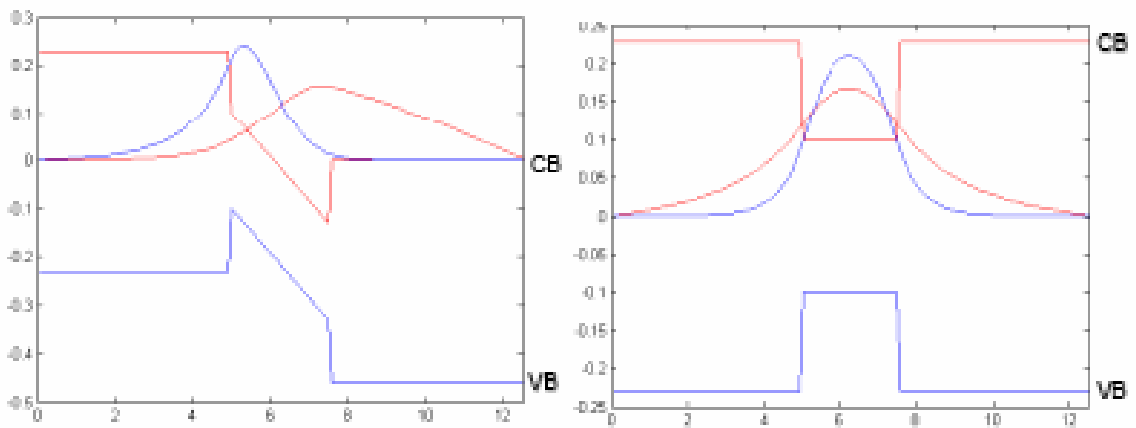

Fig. 4.15. Bandgap diagram of the InGaN/GaN QW (a) with and (b) without piezoelectric field effect.
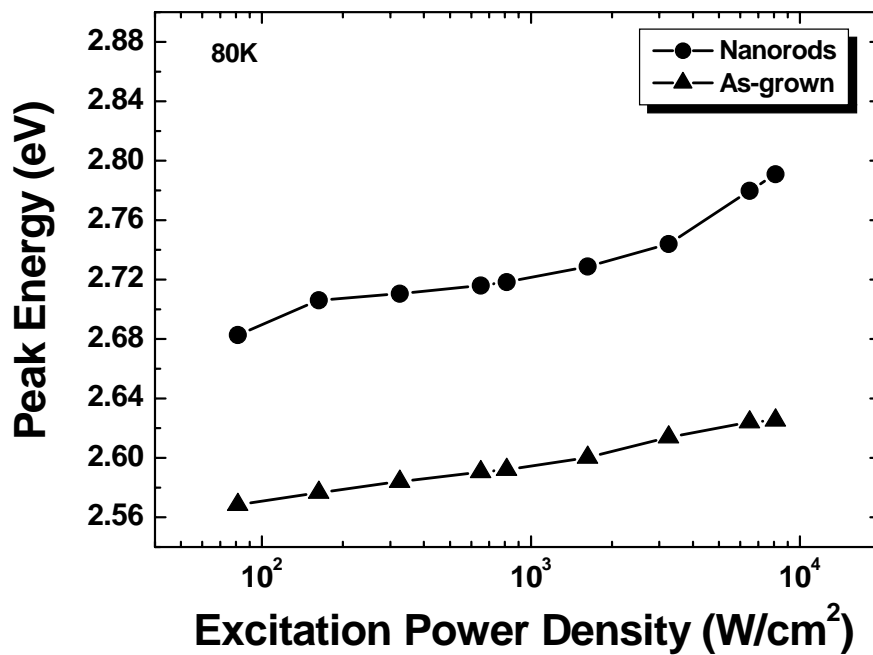
Fig. 4.16. Excitation power-density dependencies of the peak energies of nanorods and as-grown bulk samples measured at 80K.
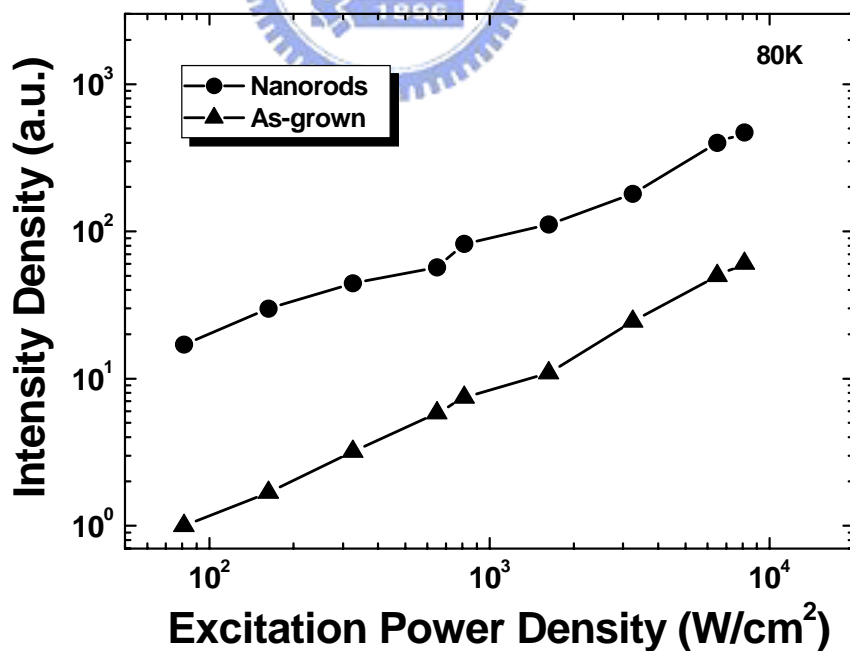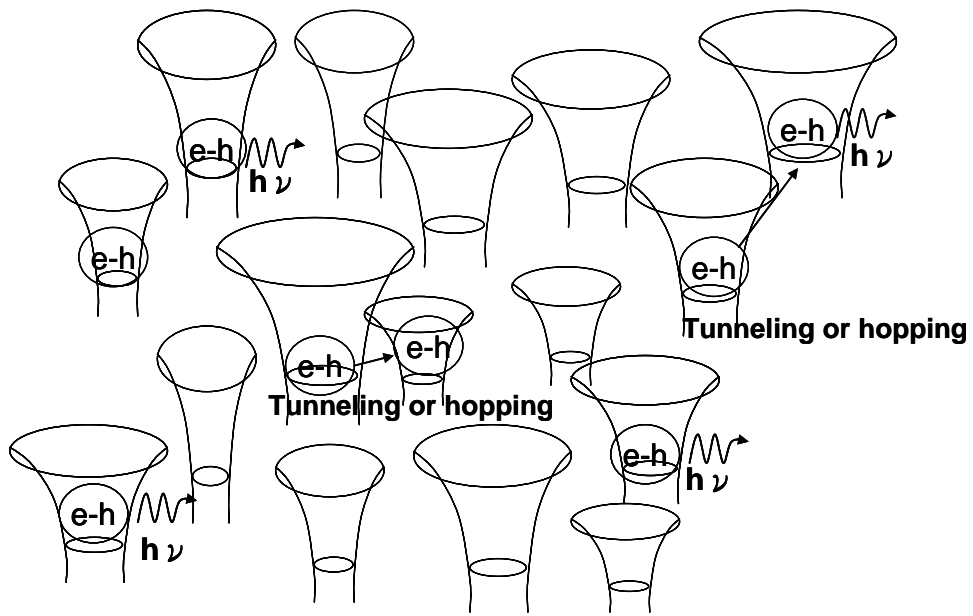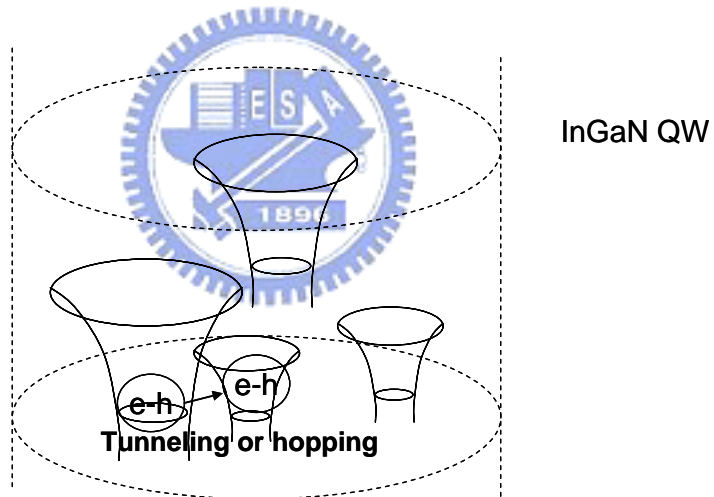

Fig. 4.17. Excitation power-density dependencies of PL emission intensity density of nanorods and as-grown bulk samples measured at 80K.

(a)

InGaN QW

(b)

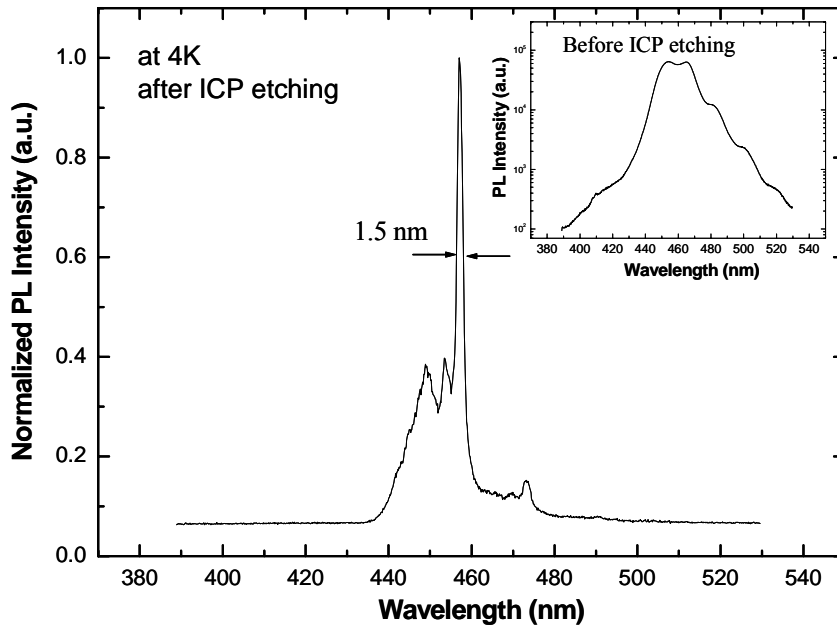Fig. 4.18. A feasible model for the dynamics of localized excitons in InGaN QW of (a) bulk and (b) nanorods structures.

Fig. 4.19. Photoluminescence spectrum of InGaN/GaN MQWs nanorods excited under 0.9 W/cm^2 at 4K. The insert is a photoluminescence spectrum of the as-grown bulk sample.
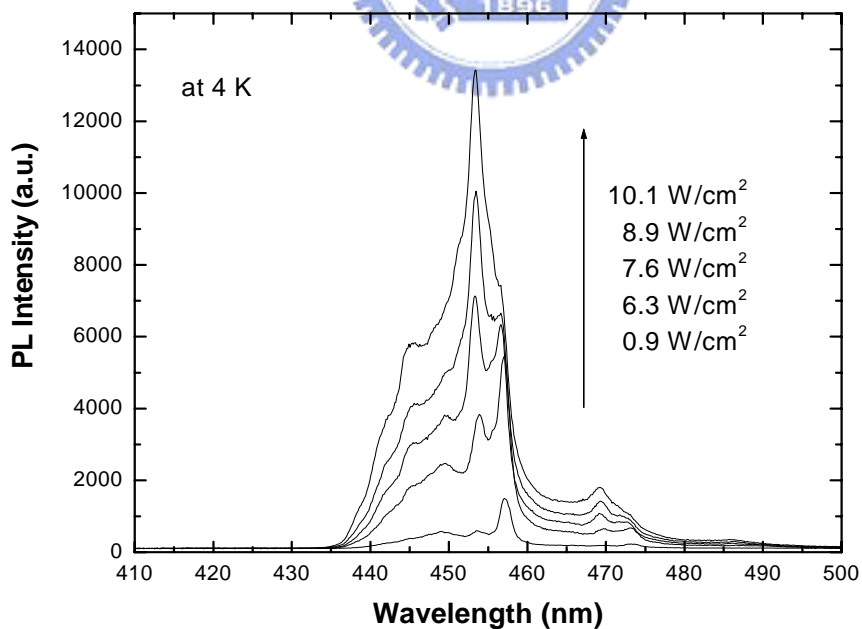

Fig. 4.20. Excitation power dependent photoluminescence spectra of InGaN/GaN MQWs nanorods at 4K.

REFERENCE

[1] C. C. Yu, C. F. Chu, J. Y. Tsai, H. W. Huang, T. H. Hsueh, C. F Lin and S. C. Wang: Jpn. J. Appl. Phys. 41, 910 (2002).

[2] W. Q. Han, S. S. Fan, Q. Q. Li and Y. D. Hu: Science 277, 1287 (1997).

[3] H. M. Kim, D. S. Kim, T. W. Kang, Y. H. Cho and K. S. Chung: Appl. Phys. Lett. 81, 2193 (2002).

[4] J. D. Carey, L. L. Ong and S. R. P. Silva: Nanotechnology 14, 1223 (2003).

[5] S. J. Pearton and R. J. Shul, in Gallium Nitride I, edited by J. I. Pankove and T. D. Moustakas (Academic, San Diego, 1998).

[6] P. Gillis, D. A. Choutov, P. A. Steiner, J. D. Piper, J. H. Crouch, P. M. Dove, and K. P. Martin, Appl. Phys. Lett. 66, 2475 (1995).

[7] R. J. Shul, in Processing of Wide Bandgap Semiconductors, edited by S. J. Pearton (Noyes, Park Ridge, NJ, 1999).

[8] I. Adesida, A. T. Ping, C. Youtsey, T. Sow, M. Asif Khan, D. T. Olson, and J. N. Kuznia, Appl. Phys. Lett. 65, 889 (1994).

[9] O. Aktas, Z. Fan, S. N. Mohammad, A. Botcharev, and H. Morkoc, Appl.Phys. Lett. 69, 25 (1996).

[10] Y. F. Wu, S. Keller, P. Kozodoy, B. P. Keller, P. Parikh, D. Kapolnek, S.P. DenBaars, and V. K. Mishra, IEEE Electron Device Lett. 18, 290 (1997).

[11] W. A. Harrison, Electronic Structure and Properties of Solids (Freeman, San Francisco, 1980).

[12] S. J. Pearton, C. R. Abernathy, F. Ren, and J. R. Lothian, J. Appl. Phys. 76, 1210 (1994).

[13] I. Adesida, A. Mahajan, E. Andideh, M. Asif Khan, D. T. Olsen, and J. N. Kuznia, Appl. Phys. Lett. 63, 2777 (1993).

[14] M. E. Lin, Z. F. Zan, Z. Ma, L. H. Allen, and H. Morkoc, Appl. Phys. Lett. 64, 887 (1994).

[15] A. T. Ping, I. Adesida, M. Asif Khan, and J. N. Kuznia, Electron. Lett. 30, 1895 (1994).

[16] H. Lee, D. B. Oberman, and J. S. Harris, Jr., Appl. Phys. Lett. 67, 1754 (1995).

[17] S. J. Pearton, C. R. Abernathy, F. Ren, J. R. Lothian, P. W. Wisk, A. Katz, and C. Constantine, Semicond. Sci. Technol. 8, 310 (1993).

[18] S. J. Pearton, C. R. Abernathy, and F. Ren, Appl. Phys. Lett. 64, 2294 (1994).

[19] R. J. Shul, G. B. McClellan, S. J. Pearton, C. R. Abernathy, C. Constantine, and C. Barratt, Electron. Lett. 32, 1408 (1996).

[20] R. J. Shul, G. B. McClellan, S. A. Casalnuovo, D. J. Rieger, S. J. Pearton, C. Constantine, C. Barratt, R. F. Karlicek, Jr., C. Tran, and M. Schurman, Appl. Phys. Lett. 69, 1119 (1996).

[21] G. F. McLane, L. Casas, S. J. Pearton, and C. R. Abernathy, Appl. Phys. Lett. 66, 3328 (1995).

[22] A. T. Ping, I. Adesida, and M. Asif Khan, Appl. Phys. Lett. 67, 1250 (1995).

[23] J. K. Sheu, G. C. Chi, and M. J. Jou, IEEE Photo. Tech. Lett. 13, 1164 (2001).

[24] R. J. Shul, in Processing of Wide Bandgap Semiconductors, edited by S.J. Pearton (Noyes, Park Ridge, NJ, 1999).

[25] S. J. Pearton, R. J. Shul, and E. Ren, MRS Internet J. Nitride Semicond. Res. 5, 11 (2000).

[26] H. K. Kim, H. Lin, and Y. Ra, J. Vac. Sci. Technol. A 22, 598 (2004).

[27] M. A. Vyvoda et al., J. Vac. Sci. Technol. A 16, 3247 (1998).

[28] M.A. Vyvoda, M. Li, D. B. Graves, H. Lee, M. V. Malyshev, F. P. Klemens, J. T. C. Lee, and V. M. Donnelly, J. Vac. Sci. Technol. B 18, 820 (2000).

[29] M. T. Bjork, B. J. Ohisson, T. Sass, A. I. Persson, C. Thelander, M. H. Magnusson, K.

Deppert, L. R. Wallenberg and L. Samuelson : Appl. Phys. Lett. 80, 1058 (2002).

[30] M. S. Gudiksen, L. J. Lauhon, J. Wang, D. C. Smith and C. M. Lieber : Nature 415, 617 (2002).

[31] W. Han, S. Fan, Q. Li and Y. Hu : Science 277, 1287 (1997).

[32] H. Peng, X. Zhou, N. Wang, Y. Zheng, L. Liao, W. Shi, C. Lee and S. Lee : Chem. Phys. Lett. 327, 263 (2000).

[33] W. Q Han and A. Zettl : Appl. Phys. Lett. 80, 303 (2002).

[34] C. Youtesy, L. T. Romano and I. Adesida : Appl. Phys. Lett. 73, 797 (1998).

[35] P. Visconti, K. M. Jones, M. A. Reshchikov, R. Cingolani, R. J. Molnar and H. Morkoc : Appl. Phys. Lett. 77, 3532 (2000).

[36] J. D. Carey, L. L. Ong and S. R. P. Silva: Nanotechnology 14, 1223 (2003).

[37] L. Dai, B. Zhang, J. Y. Lin and H. X. Jiang: J. Appl. Phys. 89, 4951 (2001).

[38] X. Duan, J. Wang and C. M. Lieber: Appl. Phys. Letts. 76, 1116 (2000).

[39] F. Bernardini, V. Fiorentini, and D. Vanderbilt, Phys. Rev. B 56, R10024 (1997).

[40] F. Bernardini and V. Fiorentini, Phys. Rev. B 57, R9427 (1998).

[41] H. Kollmer, J. S. Im, H. Kollmer, S. Heppel. J. Off, and F. Scholz, MRS Internet J. Nitride Semicond. Res. 3, 15 (1998).

[42] A. D. Bykhovski, V. V. Kaminski, M. S. Shur, Q. C. Chen, and M. A. Khan, Appl. Phys. Lett. 68, 818 (1996).

[43] K. Tsubouchi, K. Sugai, and N. Mikoshiba, Proc. IEEE 375 (1981).

[44] H.W. Choi, C. W. Jeon, M. D. Dawson, P. R. Edwards, R. W. Martin, and S. Tripathy, J. Appl. Phys. 93, 5978 (2003).

[45] L. Dai, B. Zhang, J. Y. Lin and H. X. Jiang, J. Appl. Phys. 89, 4951 (2001).

[46] J. Ristic, E. Calleja, M. A. Sanchez-Garcia, J. M. Ulloa, J. Sanchez-Paramo, J. M. Calleja, U. Jahn, A. Trampert, and K. H. Ploog, Phys. Rev. B 68, 125305 (2003).

[47] L. H. Peng, C. W. Chuang, L. H. Lou, Appl. Phys. Lett. **74,** 795 (1999).

[48] E. Kuokstis, J.W. Yang, G. Simin, M. A. Khan, R. G.aska, M. S. Shur, Appl. Phys Lett. **80,** 977 (2002).

[49] M. G. Cheong, H. S. Yoon, R. J. Choi, C. S. Kim, C.-H. Hong, E.-K. Suh, and H. J. Lee, J. Appl. Phys. 90, 5642 (2001).

[50] M. G. Cheong, C. Liu, H.W. Choi, B. K. Lee, E.-K. Suh, and H. J. Lee, J. Appl. Phys. 93, 4691 (2003).

[51] S. Nakamura and G. Fasol, The Blue Laser Diode (Springer, Berlin, 1997).

[52] Y. Narukawa, Y. Kawakami, Sz. Fujita, Sg. Fujita, and S. Nakamura, Phys. Rev. B 55, R1938 (1997).

[53] S. Chichibu, T. Azuhata, T. Sota, and S. Nakamura, Appl. Phys. Lett. 69, 4188 (1996).

[54] T. H. Hsueh, Y. S. Chang, F. Lai, H. W. Huang, M. C. Ou-yang, C. W. Chang, J. K. Sheu, H. C. Kuo, S. C. Wang, CLEO/ IQEC, IWA 20 (2004).

[55] C. C. Yu, C. F. Chu, J. Y. Tsai, H. W. Huang, T. H. Hsueh, C. F Lin and S. C. Wang, Jpn. J. Appl. Phys. 41, L910 (2002).

[56] C. Winnewisser, J. Schneider, M. Bo¨rsch, and H. W. Rotter, J. Appl. Phys. 89, 3091 (2001).

[57] K. S. Ramaiah, Y. K. Su, S. J. Chang, B. Kerr, H. P. Liu and I. G. Chen, Appl. Phys. Lett. 84, 3307 (2004).

[58] J. Ristic, E. Calleja, M. A. Sanchez-Garzia, J. M. Ullao, J. Sanchez-Paramo, J. M. Calleja, U. Jahn, A. Trampert, and K. H. Ploog, Phys. Rev. B 68, 125305 (2003).